



# Efficiently photocatalytic $H_2O$ overall splitting within the strengthened polarized field by reassembling surface single atoms

Lijun Hu<sup>a</sup>, Jiaqi Huang<sup>a</sup>, Jie Wang<sup>a</sup>, Shujuan Jiang<sup>a,\*</sup>, Chuanzhi Sun<sup>b,\*</sup>, Shaoqing Song<sup>a,\*</sup>

<sup>a</sup> School of Materials Science and Chemical Engineering, Ningbo University, Fenghua Road 818, Ningbo 315211, Zhejiang, PR China

<sup>b</sup> College of Chemistry, Chemical Engineering and Materials Science, Shandong Normal University, Jinan 250014, PR China



## ARTICLE INFO

**Keywords:**  
Single atom  
Reassembly  
 $H_2O$  overall splitting  
 $H_2$  bubbles  
Natural sunlight

## ABSTRACT

Surface single atom Ni-coordinated carbon nitride fibers (Ni/C<sub>3</sub>N<sub>4</sub>Fs) were reassembled into tiny NiP nanoparticle-integrated C<sub>3</sub>N<sub>4</sub>Fs (NiP/C<sub>3</sub>N<sub>4</sub>Fs) with the strengthened polarized electric fields accompanied by a weakened interface barrier. Photogenerated  $e^-$  and  $h^+$  dynamically transfer to the convex-integrated NiP and concave of C<sub>3</sub>N<sub>4</sub>Fs under the synergistic electric fields via inner single atoms of Ni as charge transfer bridges within C<sub>3</sub>N<sub>4</sub>Fs interlayers, which is confirmed by high-angle annular dark field scanning transmission electron microscopy, K-edge extended X-ray absorption fine structure, X-ray photoelectron spectroscopy and theoretical prediction.  $H_2$ - and  $O_2$ -evolution rates of 1.89 and 0.92 mmol g<sup>-1</sup> h<sup>-1</sup> with solar-to-hydrogen efficiency of 2.33% are obtained over NiP/C<sub>3</sub>N<sub>4</sub>Fs system under visible light irradiation. This research provides a rational strategy for constructing the connection of  $H_2$  fuel production with its practical application.

## 1. Introduction

Efficient generation of clean and green energies by solar photocatalysis has always been the dream of many scientists, in which developing hydrogen energy is particularly important owing to its high energy density and carbon-free discharge [1,2]. Once a breakthrough for photocatalytic  $H_2O$  overall splitting is achieved, predictably affecting the production and layout of global clean fuels [3]. Therefore, photocatalytic  $H_2O$  dissociating towards hydrogen fuel is considered to be one of key issues for clean energy productions (e.g., methane conversion, CO<sub>2</sub> reduction, N<sub>2</sub> fixation,  $H_2O$  splitting [4,5]. In the solar energy conversion process, recombination of  $e^-$  and  $h^+$  in bulk phase (several ps) is extremely fast in comparison with charge transfer from generation location to redox sites (hundreds of ps); on the surface, charge carrier recombination (dozens of ps) is much faster than charges involving in redox reactions (several ns ~ several ms) [6]. It is seen that, low separation efficiency of photogenerated  $e^-$  and  $h^+$  in bulk and their inferior utilization in surface reactions are key restrictive factors for solar energy conversion [7,8]. The former is always constrained by Coulomb force between  $e^-$  and  $h^+$ , and the latter is subject to a high interface barrier for charge transfer due to the different atom states and arrangements. Besides,  $H_2$  and  $O_2$  re-react easily on the surface of photocatalytic materials to form water molecules again due to the Gibbs free energy of the

reaction process ( $\Delta G^0 = -237.13 \text{ kJ mol}^{-1}$ ). Although many approaches have been tried to resolve the above key issues, e.g., loading noble co-catalysts, doping heteroatoms, constructing active crystal facets, and fabricating heterojunctions, it is far from meeting the demand of  $H_2O$  overall splitting into  $H_2$  under natural light [9,10].

Electron spin polarization field principle confirms that polarization electric field (PEF) within semiconductor noncentrosymmetry crystal structure of polar units, supplies a strong driving force for charge separation from bulk to surface [11,12]. For example, Huang et al. have reported that the orderly arrangement of IO<sub>3</sub> polar units along [001] direction in BiOIO<sub>3</sub> single crystal structure, provides a strong PEF in the opposite direction with Coulomb field, which promotes the separation and transfer of charges [13]. The constructed polarized BiOIO<sub>3</sub> single crystal presents a 10-time increased efficiency for CO<sub>2</sub> reduction to CO, becoming a good photocatalyst for CO<sub>2</sub> reduction. Kou et al. have revealed that Ag<sup>+</sup> ions within AgBiP<sub>2</sub>Se<sub>6</sub> deviate the center along z axis in ferroelectric phase due to larger radius of Ag<sup>+</sup> than the replaced Bi<sup>3+</sup>, thus forming a PEF of 0.28 Debye with a perpendicular direction to its single layer structure [14]. Under PEF action,  $h^+$  is transferred to ferroelectric phase of AgBiP<sub>2</sub>Se<sub>6</sub> for  $H_2O$  oxidation, and  $e^-$  to paraelectric phase for  $H_2O$  reduction. According to mathematical model calculation of polarization potential distribution,  $U=Q/4\pi\epsilon R$  (Q: quantity of electric charge, R: radius vector,  $\epsilon$ : dielectric coefficient), polarization potential

\* Corresponding authors.

E-mail addresses: [jiangshujuan@nbu.edu.cn](mailto:jiangshujuan@nbu.edu.cn) (S. Jiang), [suncz@sdnu.edu.cn](mailto:suncz@sdnu.edu.cn) (C. Sun), [songshaoqing@nbu.edu.cn](mailto:songshaoqing@nbu.edu.cn) (S. Song).

intensity decreases sharply when R exceeds the radius of polar unit (**Scheme S1**). Therefore, it is necessary to construct continuous electric fields in heterojunctions to greatly promote the charge separation from bulk phase to surface active sites, in which a much-reduced interface barrier is a favorable and urgent guarantee for the efficient synergy within the built multi-electric fields.

Herein, surface single atom Ni-coordinated carbon nitride fibers (Ni/C<sub>3</sub>N<sub>4</sub>Fs) were reassembled into tiny NiP nanoparticle-integrated C<sub>3</sub>N<sub>4</sub>Fs (NiP/C<sub>3</sub>N<sub>4</sub>Fs) with a weakened interface barrier as well as dual polarization electric fields (DPEFs) including spontaneous- and ferroelectric-polarized electric fields (SPEF and FPEF). With these advantages for photocatalysis, the shackles of charge transport have been completely broken under the synergistic SPEF of 0.0267 mV m<sup>-1</sup> and FPEF of 0.0144 mV m<sup>-1</sup> with the inner single atoms of Ni as charge transfer bridges. H<sub>2</sub>- and O<sub>2</sub>-evolution yieldings of 1890 and 920 μmol g<sup>-1</sup> h<sup>-1</sup> with solar-to-hydrogen (STH) efficiency of 2.33% are achieved over the optimal NiP/C<sub>3</sub>N<sub>4</sub>Fs system under visible light irradiation, which can even generate H<sub>2</sub> bubbles directly under natural solar light irradiation.

## 2. Experimental section

### 2.1. Sample preparation

Ni/C<sub>3</sub>N<sub>4</sub>Fs was prepared from single atom Ni-intercalating g-C<sub>3</sub>N<sub>4</sub> by solvothermal method (**Scheme S2**). In detail, cyanuramide (5 g, 39.5 mmol) was dispersed into an ethanol solution of C<sub>4</sub>H<sub>6</sub>O<sub>4</sub>Ni·4H<sub>2</sub>O (0.66 mM) by vigorously stirring for 4 h. After being dried at 60 °C for 12 h, the ground powder was calcined at 540 °C in a crucible with lid for 2 h at a heating rate of 5 °C min<sup>-1</sup>. The pale-yellow product was dispersed into a solution containing deionized H<sub>2</sub>O (30 mL) and ethylene glycol with ultrasonication of 2 h. Then, the suspension was heated to 180 °C in a reaction vessel and kept for 10 h. Ethylene glycol dosage was modulated from 15, 30–45 mL for diameter adjustment to C<sub>3</sub>N<sub>4</sub>F arrays based on its advantages in modifying the aspect ratio of one-dimensional semiconductors [15,16]. After washing, Ni-coordinated C<sub>3</sub>N<sub>4</sub>Fs were named as Ni/C<sub>3</sub>N<sub>4</sub>Fs-1, Ni/C<sub>3</sub>N<sub>4</sub>Fs-2, or Ni/C<sub>3</sub>N<sub>4</sub>Fs-3, respectively. Accordingly, pure C<sub>3</sub>N<sub>4</sub>F arrays with different diameters were prepared with the same method but without adding Ni source, and the obtained C<sub>3</sub>N<sub>4</sub>Fs were denoted as C<sub>3</sub>N<sub>4</sub>Fs-1, C<sub>3</sub>N<sub>4</sub>Fs-2 and C<sub>3</sub>N<sub>4</sub>Fs-3. Then Ni/C<sub>3</sub>N<sub>4</sub>Fs suffered another similar solvothermal treatment process with red phosphorus for preparation of NiP/C<sub>3</sub>N<sub>4</sub>Fs, in which Ni/C<sub>3</sub>N<sub>4</sub>Fs of 1 g and red phosphorus (3.30 mM) were dissolved in deionized water (30 mL) and ethyl alcohol (30 mL). The obtained sample was named as NiP/C<sub>3</sub>N<sub>4</sub>Fs-1, NiP/C<sub>3</sub>N<sub>4</sub>Fs-2 and NiP/C<sub>3</sub>N<sub>4</sub>Fs-3 as adopting different Ni/C<sub>3</sub>N<sub>4</sub>Fs. By this one-step hydrothermal treatment but changing Ni/C<sub>3</sub>N<sub>4</sub>Fs by C<sub>4</sub>H<sub>6</sub>O<sub>4</sub>Ni·4H<sub>2</sub>O and C<sub>3</sub>N<sub>4</sub>Fs, NiP loaded on C<sub>3</sub>N<sub>4</sub>Fs (NiP@C<sub>3</sub>N<sub>4</sub>Fs) was prepared for comparison. By inductively coupled plasma optical emission spectrometer, the actual Ni contents were detected to be 4.54 wt% (Ni/C<sub>3</sub>N<sub>4</sub>Fs-1), 4.50 wt% (Ni/C<sub>3</sub>N<sub>4</sub>Fs-2) and 4.52 wt% (Ni/C<sub>3</sub>N<sub>4</sub>Fs-3), and 3.96 wt% (NiP/C<sub>3</sub>N<sub>4</sub>Fs-1), 4.02 wt% (NiP/C<sub>3</sub>N<sub>4</sub>Fs-2) and 3.98 wt% (NiP/C<sub>3</sub>N<sub>4</sub>Fs-3), respectively.

### 2.2. Photocatalytic tests

Photocatalytic overall H<sub>2</sub>O splitting tests of the as-prepared samples were conducted in a three-neck Pyrex flask of 100 mL at ambient temperature and normal pressure under the irradiation of 300 W Xe lamp equipped with light filter of  $\lambda \geq 420$  nm (PLS-SXE300, PerfectLight). Generally, photocatalyst of 30 mg was dispersed into the deionized H<sub>2</sub>O of 100 mL under constant stirring (pH = 7). Before irradiation, N<sub>2</sub> was purged through the reaction system for 30 min to remove air and an anaerobic condition should be guaranteed. After illumination for each half hour under stirring, H<sub>2</sub> and O<sub>2</sub> yields were measured by gas chromatograph (Shimadzu GC-2014, TCD). Photocatalytic H<sub>2</sub> evolution reactions were carried out in the same experimental setup but with Na<sub>2</sub>S (0.35 mol L<sup>-1</sup>) and Na<sub>2</sub>SO<sub>3</sub> (0.25 mol L<sup>-1</sup>) as sacrificing agents.

Apparent quantum efficiency (AQE) was detected by PLR-QY1000 system. The power and wavelength of the light source were 100 mW and 420 nm, respectively, and illumination area was measured to 19.625 cm<sup>2</sup>. Moreover, the reaction system is consistent with the H<sub>2</sub>O overall splitting tests. STH was studied by 300 W Xe lamp (PLS-SXE300, PerfectLight) with a total reflection filter and an AM 1.5 G filter (100 mW cm<sup>-2</sup>) was simulated as solar light source. Light spectrum was studied by a fibre spectrometer (AvaSpec-ULS2048XL-EVO). The lighting area was set to 1.60 cm<sup>2</sup>. STH was calculated according to following equation:

$$\text{STH}(\%) = \frac{\text{Energy of generated H}_2}{\text{Solar energy irradiating the reactor}} \times 100\%$$

## 3. Results and discussion

### 3.1. Morphology and microstructure analysis

It is seen that all the three C<sub>3</sub>N<sub>4</sub>Fs samples present a compact solid structure and thus have many wrinkles on the surface, while their diameters have been well-adjusted to an average size of 2.5 ± 0.2 (C<sub>3</sub>N<sub>4</sub>Fs-1), 2.0 ± 0.2 (C<sub>3</sub>N<sub>4</sub>Fs-2), and 1.5 ± 0.2 μm (C<sub>3</sub>N<sub>4</sub>Fs-3) by modulating the ethylene glycol dosages in synthesis process, as recorded by morphology observation in field emission scanning electron microscopy (FESEM) and transmission electron microscopy (TEM) (**Fig. S1**). Ni/C<sub>3</sub>N<sub>4</sub>Fs seems no much difference in morphology to C<sub>3</sub>N<sub>4</sub>Fs, but Ni single atoms have been clearly presented as many tinny lightdots with a size of ~0.3 nm in high-angle annular dark field scanning transmission electron microscopy (HAADF-STEM) (**Fig. 1A-D**, **Fig. S2A&B**). The interaction of single atom Ni with C<sub>3</sub>N<sub>4</sub>Fs was further revealed by X-ray absorption near edge spectra (XANES) and Fourier transform extended X-ray absorption fine structure spectrum (FT-EXAFS), in which standard Ni foil and NiO samples were selected as references. In XANES of Ni K-edge result, Ni/C<sub>3</sub>N<sub>4</sub>Fs has an absorption edge at 8349.71 eV, which is positive to Ni foil (8349.29 eV) but similar to NiO (8349.79 eV). This means that single atom Ni is in a high valence state in Ni/C<sub>3</sub>N<sub>4</sub>Fs. Furthermore, single atom Ni displays a much different coordinated environment to NiO, as revealed by its only one predominant coordination peak with a fitted bond length of ~ 1.53 Å in R-space for Ni-N bonds compared with those of ~ 2.59 Å for Ni-Ni and ~ 1.64 Å for Ni-O bonds in NiO reference of FT-EXAFS, and further quantitative EXAFS curve fitting analyses for Ni/C<sub>3</sub>N<sub>4</sub>Fs confirm that the coordination numbers of the first coordination sphere in the Ni center are estimated to be ~5.0 at the distance of ~2.04 Å for Ni-N shell (**Fig. 1E&F**, **Table S1**) [17]. It hence can be confirmed that for Ni/C<sub>3</sub>N<sub>4</sub>Fs, single atoms of Ni have been coordinated with *sp*<sup>2</sup>-hybridized N of C<sub>3</sub>N<sub>4</sub>Fs. After phosphorization, some nanoparticles with sizes of ~4–7 nm appear on the surface of NiP/C<sub>3</sub>N<sub>4</sub>Fs sample (**Fig. 1G**, and **Fig. S2C-G**). The following HAADF-STEM observation confirms that surface Ni single atoms have been converted to NiP facilely, while those confined within C<sub>3</sub>N<sub>4</sub>Fs can be protected and thus keep at the state of single atoms due to the tightly curved structure of C<sub>3</sub>N<sub>4</sub>Fs. In HAADF-STEM images for NiP/C<sub>3</sub>N<sub>4</sub>Fs, it is seen that the inner tiny lightdots of single atom Ni still exist widely; meanwhile, several sparse big nanoparticles appear on the edge of the sample. The exposed lattice fringe spacing of these nanoparticles is measured to be 0.221 nm, which corresponds to the (111) crystal facet of hexagonal phase NiP (**Fig. 1H**, and **Fig. S3**) [18,19]. Subsequently, X-ray photoelectron spectroscopy (XPS) was performed to investigate changes of chemical environment for Ni, N, and P before and after reassembling (**Fig. 1I&J**). For NiP/C<sub>3</sub>N<sub>4</sub>Fs, the binding energy (BE) at 129.6 eV of P 2p spectrum is assigned to the Ni-P species [20], while the obvious characteristic signals for Ni-N species both in N 1 s and Ni 2p of NiP/C<sub>3</sub>N<sub>4</sub>Fs and Ni/C<sub>3</sub>N<sub>4</sub>Fs can be detected. Notably, these signals in NiP/C<sub>3</sub>N<sub>4</sub>Fs present a positive or negative shift compared with those in Ni/C<sub>3</sub>N<sub>4</sub>Fs. In detail, the peak for N-Ni signal in N 1 s spectra of Ni/C<sub>3</sub>N<sub>4</sub>Fs shifts positively from 398.0 eV to 398.2 eV in NiP/C<sub>3</sub>N<sub>4</sub>Fs, while the unsaturated Ni species of Ni<sup>δ+</sup> 2p<sub>3/2</sub> shifts negatively from

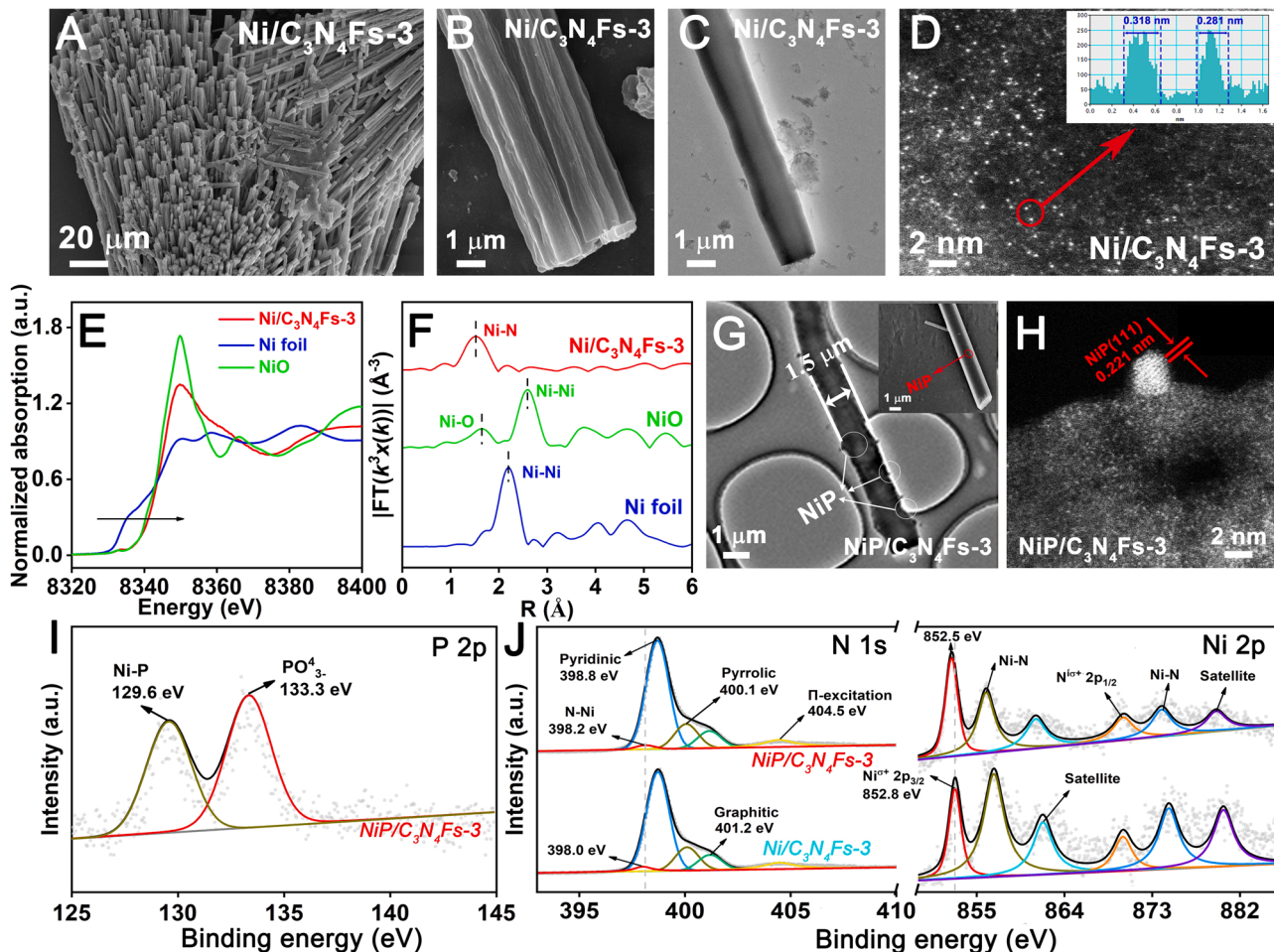


**Fig. 1.** Morphology and microstructure analysis. (A, B) FESEM, (C) TEM and (D) HAADF-STEM images for Ni/C<sub>3</sub>N<sub>4</sub>Fs-3. (E) Normalized XANES spectra and (F) FT-EXAFS spectra for Ni/C<sub>3</sub>N<sub>4</sub>Fs-3. (G) TEM, SEM (insert), and (H) HAADF-STEM images for NiP/C<sub>3</sub>N<sub>4</sub>Fs-3. (I) P 2p XPS spectrum for NiP/C<sub>3</sub>N<sub>4</sub>Fs-3. (J) N 1s and Ni 2p XPS spectra for Ni/C<sub>3</sub>N<sub>4</sub>Fs-3 and NiP/C<sub>3</sub>N<sub>4</sub>Fs-3.

852.8 eV to 852.5 eV due to the participation of P with low electronegativity into surface single atom reassembling partially instead of N with high electronegativity [21,22]. Along with the change of peak positions, the reduced peak intensity of Ni-N in Ni/C<sub>3</sub>N<sub>4</sub>Fs and the increased one of Ni<sup>δ+</sup> in NiP/C<sub>3</sub>N<sub>4</sub>Fs also indicate the phosphating process, and thus an approximate phosphating degree of 10.7–29.7% can be evaluated from the peak area proportion changes and Ni content in samples (Table S2). Combined with P 2p, N 1s and Ni 2p spectra in XPS, it can be confirmed that the surface single atoms of Ni have been converted to NiP with a strong interaction with C<sub>3</sub>N<sub>4</sub>Fs in the form of N-Ni-P species, and inner single atoms of Ni within C<sub>3</sub>N<sub>4</sub>Fs interlayers have been retained.

### 3.2. DPEF formation and intensity determination

In light of the obtained morphology and microstructure, molecular theoretical calculation models of C<sub>3</sub>N<sub>4</sub>F, g-C<sub>3</sub>N<sub>4</sub> and NiP composite were set up, in which C<sub>3</sub>N<sub>4</sub>F configuration was constructed and optimized with using three curved heptazine units linked via the delocalized  $sp^2$ -hybridized N. For planar g-C<sub>3</sub>N<sub>4</sub>, equipotential lines are homogeneously and symmetrically distributed around heptazine unit plane because of delocalization property of  $\pi$  electrons (Fig. 2A). Deviation from g-C<sub>3</sub>N<sub>4</sub> plane results in partial hybridization of C and N from  $sp^2$  to  $sp^3$  in the curved delocalized heptazine units [23,24]; in this case,  $\pi$  electrons spontaneously migrate from concavity to convexity, as reflected by the asymmetrical distribution of equipotential curves for C<sub>3</sub>N<sub>4</sub>Fs (Fig. 2B).

Obviously, equipotential lines of C<sub>3</sub>N<sub>4</sub>F are more concentrated on convexity than in concave (insert in Fig. 2B), meaning a SPEF has been formed. Under the action of SPEF, photoexcited  $e^-$  tends to transfer to convexity, while  $h^+$  to concavity. When NiP anchors on g-C<sub>3</sub>N<sub>4</sub>, saturation magnetization increases from nonmagnetic property for C<sub>3</sub>N<sub>4</sub>Fs to 0.78 emu g<sup>-1</sup> for NiP/C<sub>3</sub>N<sub>4</sub>Fs-3 in magnetic hysteresis loop tests (Fig. 2C). Meanwhile, strong charge interaction within the interface of NiP and g-C<sub>3</sub>N<sub>4</sub> occurs, and the electron gaining (yellow region) or losing (blue region) is reflected by differential charge distribution analysis due to the different work functions between g-C<sub>3</sub>N<sub>4</sub>(001) (4.24 eV) and NiP(111) (5.25 eV) (Fig. 2D&E, Fig. S4). Owing to the higher Fermi level of g-C<sub>3</sub>N<sub>4</sub>(001) than that of NiP(111), negative charges tend to concentrate around NiP, while positive charges to g-C<sub>3</sub>N<sub>4</sub>, as revealed by the asymmetrical distribution of positive (blue) and negative (yellow) charges in planar-average charge density (Fig. 2F), confirming a FPEF has been generated [25,26].

Furthermore, SPEF and FPEF were experimentally detected by electrochemical impedance spectroscopy (EIS, Fig. S5A) and derived by Eqs. (1–5). The process is as follows:

$$\omega = 2\pi f \quad (1)$$

$$C = -\frac{1}{w * Z''} \quad (2)$$

$$C = \frac{S * \epsilon}{4\pi k d} \quad (3)$$

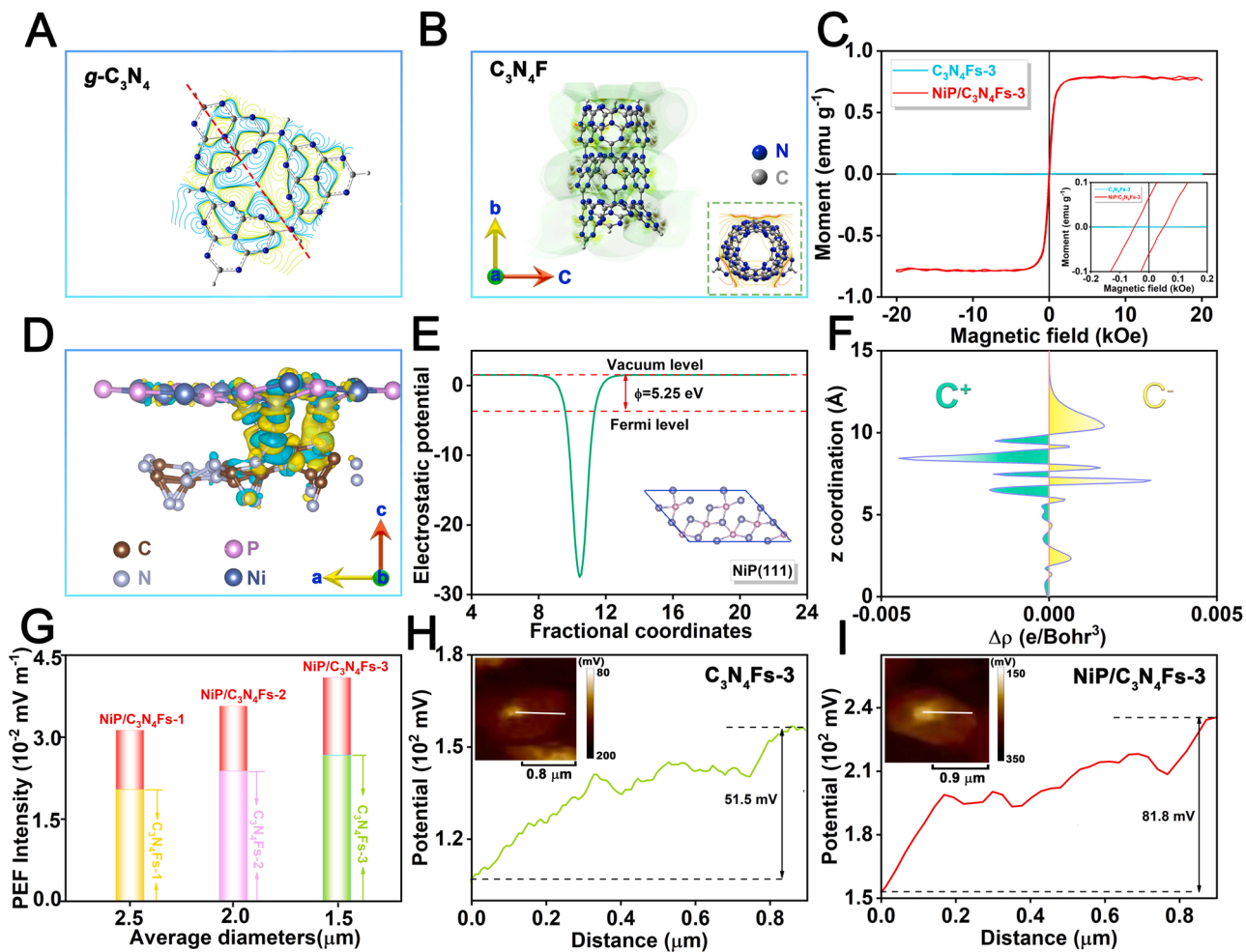


**Fig. 2.** DPEF formation and intensity determination. (A,B) Equipotential curve distribution for  $g\text{-C}_3\text{N}_4$  (A) and  $\text{C}_3\text{N}_4\text{F}$  (B). (C) Magnetic hysteresis loops of  $\text{C}_3\text{N}_4\text{Fs-3}$  and  $\text{NiP/C}_3\text{N}_4\text{Fs-3}$ . (D) Differential charge distribution, yellow region indicates electron gaining and blue region means charge losing. (E) Work function for  $\text{NiP}(111)$ . (F) Planar-average charge density, yellow region indicates electron gaining and blue region means charge losing. (G) PEF intensity calculated from EIS. (H,I) Potential changes in KPFM along with the scanning route in AFM images (insets) for  $\text{C}_3\text{N}_4\text{Fs-3}$  (H) and  $\text{NiP/C}_3\text{N}_4\text{Fs-3}$  (I).

Eq. (4) can be obtained by Eqs. (1–3):

$$f = \frac{2kd}{S * \epsilon} \left( -\frac{1}{Z''} \right) \quad (4)$$

In these equations,  $k$  is electrostatic constant;  $d$ , sample thickness;  $S$ , sample area;  $\epsilon$ , relative permittivity;  $f$ , impedance frequency;  $Z''$ , the imaginary part of impedance. Combining  $f \sim -\frac{1}{Z''}$  with the slope  $K = \frac{2kd}{S * \epsilon}$  (Fig. S5B), relative permittivity  $\epsilon$  can be calculated. According to the relationship between  $\epsilon$  and the electric field intensity ( $E'$ ) (Eq. 5), SPEF and FPEF values can be obtained (Fig. 2G) [27,28]:

$$\epsilon = \frac{E_0}{E_0 - E'} \quad (5)$$

$E_0$  is applied electric field and  $E'$ , the polarized electric field. It is seen that SPEF intensity increases with decreasing the diameter of  $\text{C}_3\text{N}_4\text{Fs}$ , i.e., SPEF intensity is 0.0204, 0.0239, and 0.0267  $\text{mV m}^{-1}$  for  $\text{C}_3\text{N}_4\text{Fs-1}$ ,  $\text{C}_3\text{N}_4\text{Fs-2}$ , and  $\text{C}_3\text{N}_4\text{Fs-3}$ , respectively. Subsequently, when ferroelectric NiP was anchored on  $\text{C}_3\text{N}_4\text{Fs}$  with the same loading, polarization field intensity presented an increment of the same magnitude ( $0.0124 \text{ mV m}^{-1}$ ) to 0.0314, 0.0358 and 0.0411  $\text{mV m}^{-1}$  for  $\text{NiP/C}_3\text{N}_4\text{Fs-1}$ ,  $\text{NiP/C}_3\text{N}_4\text{Fs-2}$ ,  $\text{NiP/C}_3\text{N}_4\text{Fs-3}$ , respectively. Furthermore, PEF intensities and directions within  $\text{C}_3\text{N}_4\text{Fs}$  and  $\text{NiP/C}_3\text{N}_4\text{Fs}$  were also detected by atomic force microscopy (AFM) combined with Kelvin probe force microscopy (KPFM) (Fig. 2H&I) [29]. It is found that scanning along the line from the radial center to surface, the potential increases by

51.5 mV for  $\text{C}_3\text{N}_4\text{Fs}$ , while an enhancement of 81.8 mV for  $\text{NiP/C}_3\text{N}_4\text{Fs}$ , indicating the formation of SPEF with the direction pointing from surface to radial center of  $\text{C}_3\text{N}_4\text{Fs}$  and also a strengthened PEF within  $\text{NiP/C}_3\text{N}_4\text{Fs}$ . Therefore, under this dual polarization electric fields, photogenerated electrons will be driven to transfer from inner side of  $\text{C}_3\text{N}_4\text{Fs}$  to outer NiP component smoothly and continuously through Ni-N bridges during photocatalytic  $\text{H}_2\text{O}$  splitting reaction.

### 3.3. Influence of DPEFs on charge transfer and photoelectric conversion

Soon afterwards, efficient charge transfer and good conduction performance of  $\text{C}_3\text{N}_4\text{Fs}$ -based samples were directly detected by Hall effect tests (Fig. 3A) [30,31]. It is seen that an increasing Hall mobility efficiency and charge carrier concentration as well as a decreasing resistivity have been obtained from  $\text{C}_3\text{N}_4\text{Fs-1}$  to  $\text{NiP/C}_3\text{N}_4\text{Fs-1}$  and further to  $\text{NiP/C}_3\text{N}_4\text{Fs-3}$ , and these parameters over  $\text{NiP/C}_3\text{N}_4\text{Fs}$  samples become more and more favorable for electron transfer as the diameter of  $\text{C}_3\text{N}_4\text{Fs}$  decreases. It can also be reflected by the longest charge lifetime in transient photoluminescence (PL) and the lowest intensity in steady-state PL spectra of  $\text{NiP/C}_3\text{N}_4\text{Fs-3}$  among all samples (Fig. 3B&C, and Table S3) [32,33]. In this process,  $e^-$  transfers from bulk phase of  $\text{C}_3\text{N}_4\text{Fs}$  to its convex surface and ultimately to the anchored NiP under the action of smooth DPEFs with a decreased interface barrier via Ni-N bonds as  $e^-$  transfer bridges, while  $h^+$  moves to the radial center of  $\text{NiP/C}_3\text{N}_4\text{Fs}$ . As a result, efficient charge separation can be achieved over

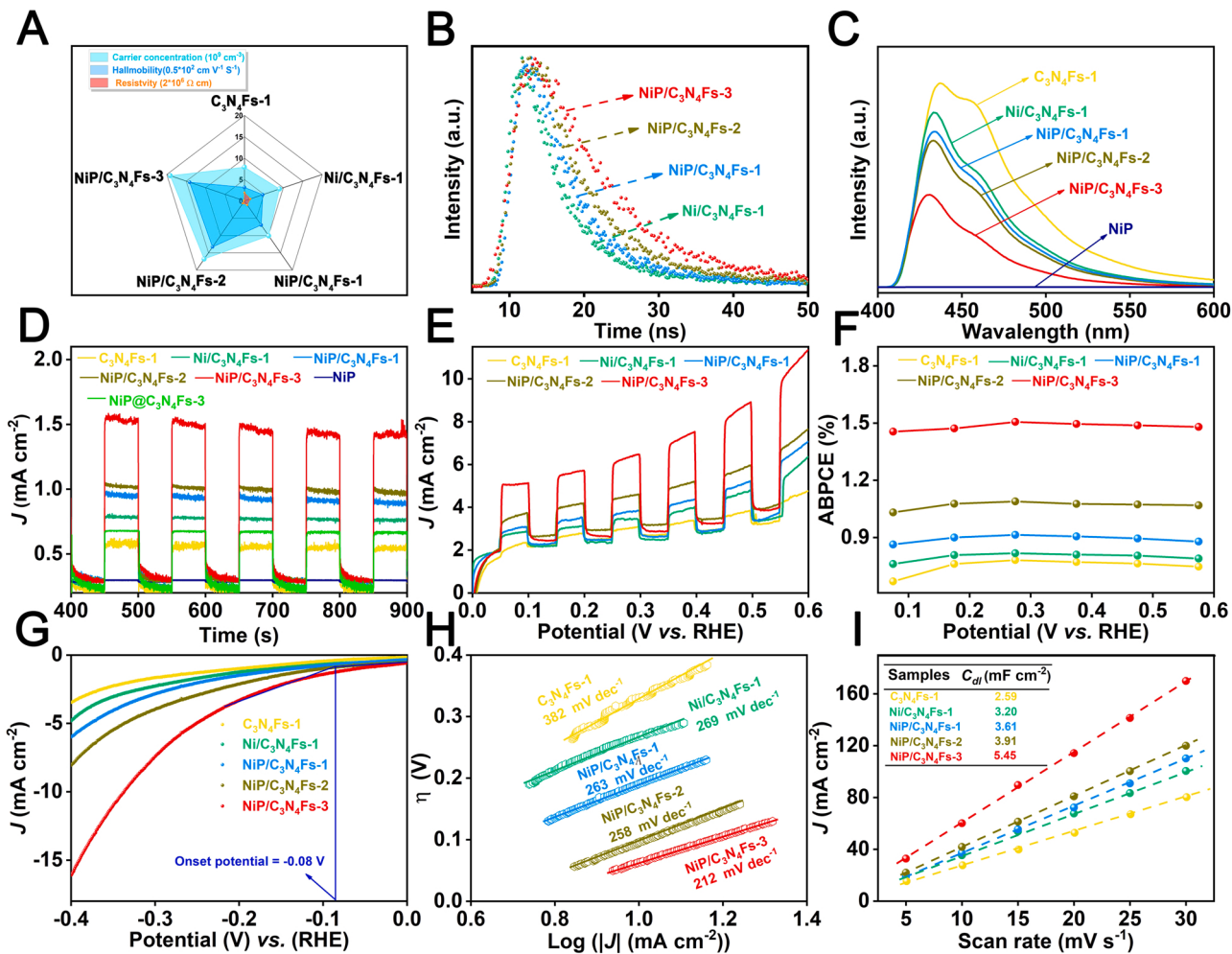


**Fig. 3.** Influence of DPEFs on charge transfer and photoelectric conversion. (A) Hall effect parameters. (B) Transient PL emission spectra. (C) Steady-state PL spectra. (D) Transient photocurrent responses. (E,F) Chopped J-V curves and the derived ABPCE data from J-V curves. (G,H) Linear sweep voltammogram curves and the converted Tafel slope plots. (I) Double-layer electrical capacitance curves.

$\text{C}_3\text{N}_4\text{Fs}$ -based samples, which contributes the highest efficiency to  $\text{NiP/C}_3\text{N}_4\text{Fs-3}$  due to the strengthened SPEF with decreasing diameter of  $\text{C}_3\text{N}_4\text{Fs}$ .

Meanwhile, the band structure of  $\text{C}_3\text{N}_4\text{Fs}$  has been revealed by UV-vis diffuse reflectance spectra and Mott-Schottky plots (Fig. S5C-H). It is seen that quantum confinement effect results in a blue shift for light absorption edge along from  $\text{C}_3\text{N}_4\text{Fs-1}$  to  $\text{C}_3\text{N}_4\text{Fs-3}$  with an expanding excitation energy from 2.90 to 2.96 eV. In this changing process, Coulomb electric field is decreasing, while DPEFs are increasing with reducing radius of  $\text{C}_3\text{N}_4\text{Fs}$ , and hence photons will be more effectively converted into photogenerated charge carriers under irradiation [34]. As expected, under simulated sunlight excitation ( $\lambda \geq 420 \text{ nm}$ ), photons will be efficiently transformed into electrons and accumulated into high photocurrent density with a good stability in chronoamperometry i-t tests (Fig. 3D) as well as chopped J-V curves (Fig. 3E).  $J$  of  $5.17 \text{ mA cm}^{-2}$  over  $\text{NiP/C}_3\text{N}_4\text{Fs-3}$  in chopped J-V curve is more than 1.79 times compared with that of  $\text{Ni/C}_3\text{N}_4\text{Fs-1}$  at  $0.10 \text{ V}$  vs. RHE, and the deduced applied bias photon-to-current efficiency (ABPCE) is 1.51% (Fig. 3F). Strong photo-electric conversion ability boosts  $\text{H}_2\text{O}$  splitting at a low onset potential of  $-0.08 \text{ V}$  vs. RHE in linear sweep voltammogram tests of  $\text{NiP/C}_3\text{N}_4\text{Fs-3}$  confirmed by the tangent method (Fig. 3G), indicating an activated surface and thus the decreased charge transfer barrier [35,36]. Moreover, the rate-determining step is confirmed to be Volmer reaction process over  $\text{NiP/C}_3\text{N}_4\text{Fs}$  samples derived from Tafel slopes above  $120 \text{ mV dec}^{-1}$  (Fig. 3H), meaning that  $\text{H}_2\text{O}$  adsorption and

electron transportation efficiency play decisive roles in  $\text{H}_2\text{O}$  splitting into  $\text{H}_2$  [37]. Besides, larger Brunauer-Emmett-Teller specific area as well as electrochemical active areas are also obtained over  $\text{NiP/C}_3\text{N}_4\text{Fs-3}$ , meaning more active sites can be exposed to reactants (Fig. 3I, Fig. S6&7, Table S4). As it is seen, significantly efficient charge separation and transfer ability as well as strong surface interaction for  $\text{NiP/C}_3\text{N}_4\text{Fs}$  with dual polarization electric fields will certainly reduce  $\text{H}_2\text{O}$  splitting barrier and boost solar energy conversion into  $\text{H}_2$  fuel, which is confirmed by the subsequent photocatalytic  $\text{H}_2\text{O}$  overall splitting.

#### 3.4. Photocatalytic capability for $\text{H}_2\text{O}$ overall splitting

Photocatalytic  $\text{H}_2\text{O}$  splitting into  $\text{H}_2$  tests over samples (30 mg with mass optimization tests) were performed in a three-neck glass reactor with or without sacrificial agents under the irradiation of  $\lambda \geq 420 \text{ nm}$  (Fig. 4, Fig. S8A&B). It is found that  $\text{C}_3\text{N}_4\text{F}$  arrays show no photocatalytic performance for  $\text{H}_2\text{O}$  overall splitting, while single atom Ni introduction promotes water splitting reaction in a certain degree, as shown by the increasing  $\text{H}_2$  and  $\text{O}_2$  yielding efficiency of  $0.26/0.10$  ( $\text{Ni/C}_3\text{N}_4\text{Fs-1}$ ),  $0.48/0.20$  ( $\text{Ni/C}_3\text{N}_4\text{Fs-2}$ ) and  $0.63/0.30 \text{ mmol g}^{-1} \text{ h}^{-1}$  ( $\text{Ni/C}_3\text{N}_4\text{Fs-3}$ ) along with decreasing  $\text{C}_3\text{N}_4\text{F}$  diameter (Fig. 4A, Fig. S8C). Notably, when surface Ni single atoms are reassembled into  $\text{NiP}$  nanoparticles,  $\text{NiP/C}_3\text{N}_4\text{Fs}$  samples have significantly boosted photocatalytic activities within the constructed DPEFs, i.e., the  $\text{H}_2$ - and  $\text{O}_2$ -evolution

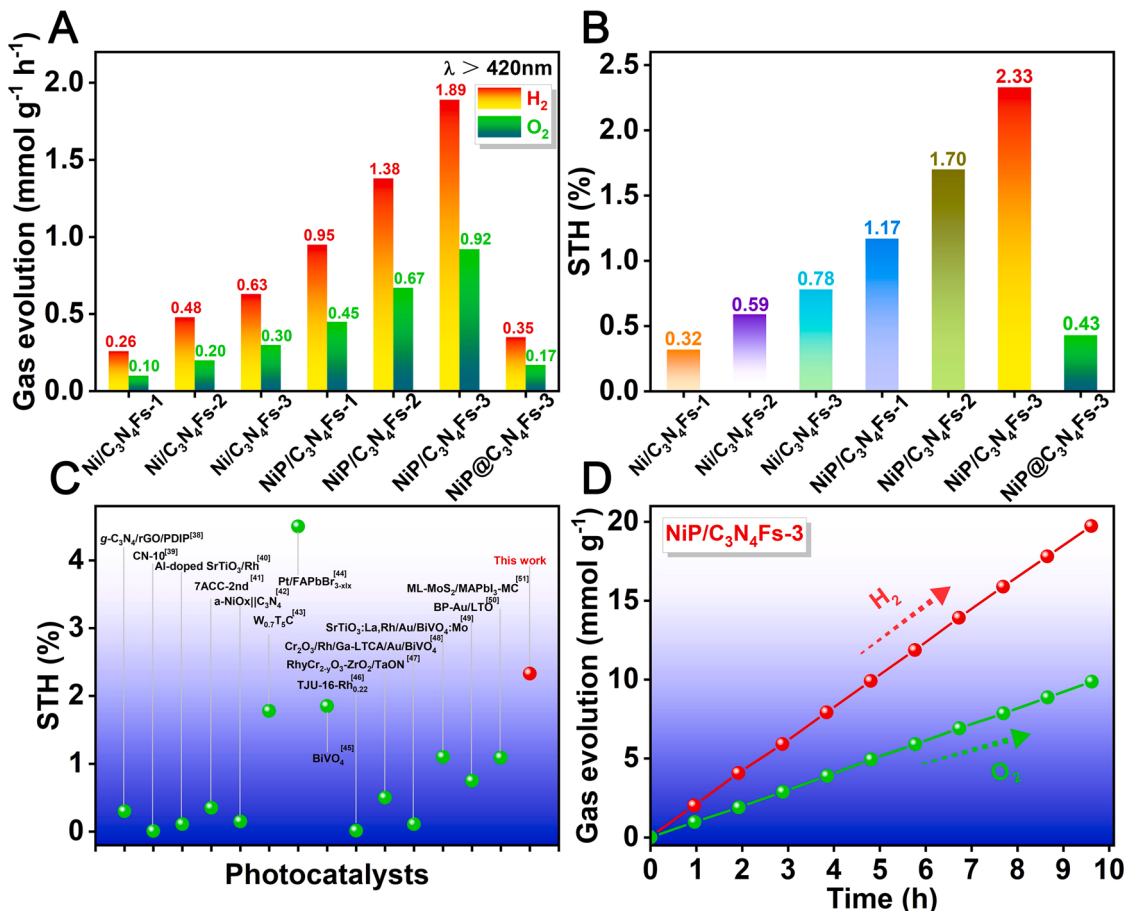


**Fig. 4.** Photocatalytic capability for  $\text{H}_2\text{O}$  overall splitting. (A) Overall water splitting activities under irradiation of  $\lambda > 420\text{ nm}$ . (B) STH of samples. (C) Comparison of STH for NiP/C<sub>3</sub>N<sub>4</sub>Fs-3 with the reported photocatalysts. (D)  $\text{H}_2$  and  $\text{O}_2$  yield curves vs. irradiation time over NiP/C<sub>3</sub>N<sub>4</sub>Fs-3.

performances are 0.95/0.45, 1.38/0.67, and 1.89/0.92  $\text{mmol g}^{-1} \text{h}^{-1}$  corresponding to NiP/C<sub>3</sub>N<sub>4</sub>Fs-1, NiP/C<sub>3</sub>N<sub>4</sub>Fs-2, and NiP/C<sub>3</sub>N<sub>4</sub>Fs-3, respectively. In contrast, NiP@C<sub>3</sub>N<sub>4</sub>Fs-3 shows a much poor efficiency compared with NiP/C<sub>3</sub>N<sub>4</sub>Fs-3 because of its inherent large interface barrier between the large and uneven NiP particles and C<sub>3</sub>N<sub>4</sub>Fs as well as the deficiency of single atom Ni as charge transfer bridge (Fig. S8D&E). Meanwhile, NiP/C<sub>3</sub>N<sub>4</sub>Fs-3 has great advantage for water splitting in comparison with recent materials supporting noble metals (Fig. S8F and Table S5) [25,38,46]. The photocatalysis over NiP/C<sub>3</sub>N<sub>4</sub>Fs-3 under simulated solar light irradiation has been videoed, and the representative video data of photocatalytic system is shown as Video S1. Gas bubbles are releasing continuously ( $\lambda \geq 420\text{ nm}$ ); as the light source is covered up, bubbles go away. Along with photocatalysis proceeding,  $\text{H}_2$  evolution amounts over NiP/C<sub>3</sub>N<sub>4</sub>Fs photocatalysts are in proportion to irradiation time with a large curve slope for NiP/C<sub>3</sub>N<sub>4</sub>Fs-3, and  $\text{H}_2$  evolution yield increases to 5.61  $\text{mmol g}^{-1}$  within 3 h (Fig. S8G). Amazingly, when moved the reaction system to outdoor and irradiated with natural sunlight (intensity: 2.62  $\text{mW cm}^{-2}$ , Ningbo city, May), NiP/C<sub>3</sub>N<sub>4</sub>Fs-3 system can generate a great number of bubbles continuously (Video S2), indicating its application prospect.

Supplementary material related to this article can be found online at doi:10.1016/j.apcatb.2022.121945.

Supplementary material related to this article can be found online at doi:10.1016/j.apcatb.2022.121945.

Moreover, AQE at 420 nm and STH under visible-light irradiation for  $\text{H}_2\text{O}$  overall splitting are detected and calculated to be 12.50% and 2.33% for NiP/C<sub>3</sub>N<sub>4</sub>Fs-3, respectively, and the STH value is higher than most of the reported representative photocatalysts (Fig. 4B&C, Fig. S8H) [38–51], suggesting the much efficient transfer and utilization of

photogenerated charges as well as their greatly effective conversion into chemical energy with DPEF promotion. Furthermore, NiP/C<sub>3</sub>N<sub>4</sub>Fs demonstrates stable and persistent photocatalytic performance in continuous  $\text{H}_2\text{O}$  overall splitting test for 10 h (Fig. 4D). Besides, in recycling tests, no obvious decrease in photocatalytic activity was observed after five recycling tests, indicating that NiP/C<sub>3</sub>N<sub>4</sub>Fs shows a high reusable performance for converting solar energy into clean energy through characterizations of morphology and chemical state before and after the photocatalysis (Fig. S9).

To reveal the inherent mechanism for the enhanced photocatalytic  $\text{H}_2\text{O}$  overall splitting, single particle PL technique is adopted to test PL images and intensities of single fiber in water so as to *in situ* probe the transfer and utilization efficiencies of the photogenerated charges over different sections of Ni/C<sub>3</sub>N<sub>4</sub>Fs-3 or NiP/C<sub>3</sub>N<sub>4</sub>Fs-3 (Scheme S3). In comparison with PL images of Ni/C<sub>3</sub>N<sub>4</sub>Fs-3 (Fig. 5A&B), it is seen that the brightness of NiP/C<sub>3</sub>N<sub>4</sub>Fs-3 as a whole is obviously weaker than that of Ni/C<sub>3</sub>N<sub>4</sub>Fs-3, suggesting that PL has been quenched to a higher level over the former than the latter, and thus the efficiencies of charge transfer and utilization in reactions have been much improved in NiP/C<sub>3</sub>N<sub>4</sub>Fs system [52]. Meanwhile, the brightness at cross sections is significantly stronger than that on the convex surface for both samples, indicating that reaction rates and kinetics of  $\text{H}_2\text{O}$  molecules with  $e^-$  on convex surfaces and  $h^+$  on cross sections are much different. From PL data (Fig. 5C), with surface single atom phosphorization, the quenching efficiency of Ni/C<sub>3</sub>N<sub>4</sub>Fs-3 has been improved by 7.07 and 6.48 folds for  $e^-$  on convexity and  $h^+$  at cross sections, respectively, which also indicates that kinetics of  $\text{H}_2\text{O}$  oxidation with  $h^+$  at cross sections is more difficult than that of  $\text{H}_2\text{O}$  reduction with  $e^-$  on convex surface. Meanwhile, this phenomenon and essence are also reflected by the

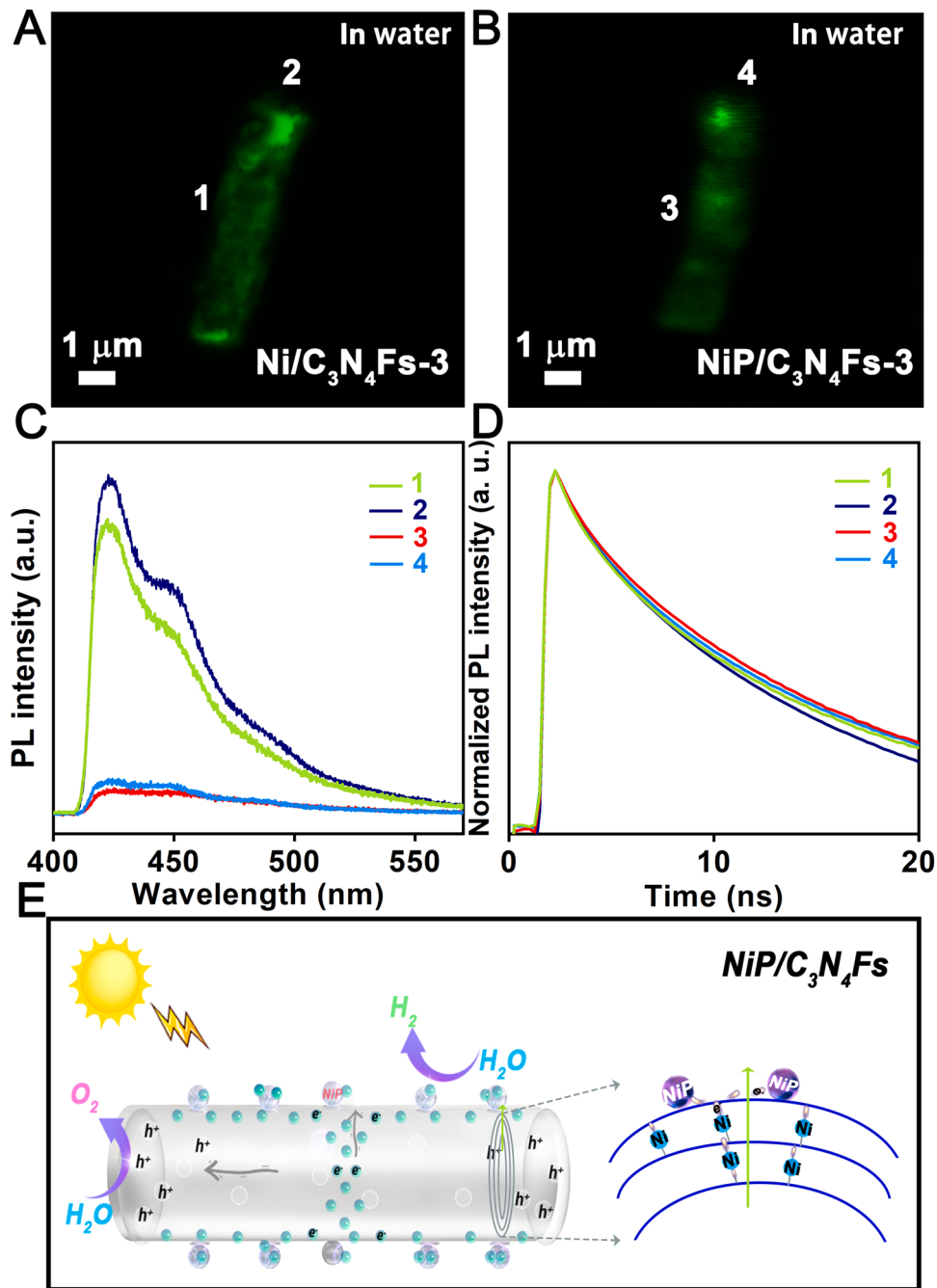


**Fig. 5.** (A,B) Single-particle PL images for  $\text{Ni/C}_3\text{N}_4\text{Fs-3}$  and  $\text{NiP/C}_3\text{N}_4\text{Fs-3}$ , and the corresponding (C) *in situ* PL spectra and (D) transient PL spectra. (E) The schematic diagram for electron transfer of the photocatalytic reaction mechanism.

photogenerated charge lifetime in transient PL spectra (Fig. 5D). In photocatalytic process (Fig. 5E), photogenerated  $e^-$  moves from bulk phase of  $\text{C}_3\text{N}_4\text{Fs}$  to their convex surface through the inner single atom Ni-N bridges, and then further migrates to NiP active sites smoothly and successfully under DPEFs action; In this case, these photogenerated  $e^-$  can react with  $\text{H}_2\text{O}$  to produce  $\text{H}_2$ ; meanwhile  $h^+$  moves from generation sites to cross sections of  $\text{C}_3\text{N}_4\text{Fs}$  to oxidize  $\text{H}_2\text{O}$  and yield  $\text{O}_2$ .

#### 4. Conclusion

In summary, single atom Ni-coordinated on the surface of carbon nitride fibers have been reassembled into tiny NiP nanoparticle-integrated  $\text{C}_3\text{N}_4\text{Fs}$ . Series of characterizations and theoretical predictions confirm that the kinetic shackles of charge transport have been

solved over the constructed system based on the following properties: i) a weakened interface barrier between the integrated NiP and  $\text{C}_3\text{N}_4\text{Fs}$ ; ii) synergistic dual polarization electric fields including SPEF and FPEF within the system; iii) the inner single atom Ni-N bridges for photogenerated charge transfer. Under visible light irradiation,  $\text{H}_2$ - and  $\text{O}_2$ -evolution rates of  $1890$  and  $920 \mu\text{mol g}^{-1} \text{h}^{-1}$  with STH of  $2.33\%$  are obtained on convex-integrated NiP and cross sections of the optimized  $\text{NiP/C}_3\text{N}_4\text{Fs}$ , respectively. The research explores a strategy that constructs dual polarization electric fields along with a weakened interface barrier for  $\text{H}_2\text{O}$  overall splitting, greatly promoting commercialization developments of solar energy conversion into chemical fuels.

## CRediT authorship contribution statement

**Lijun Hu:** Conducting experiments, Collecting data, Writing – original draft. **Jiaqi Huang:** Conducting supplementary experiments. **Jie Wang:** Conducting supplementary experiments. **Shujuan Jiang:** Ideas, Revising manuscript. **Chuanzhi Sun:** Theoretical calculation and data analysis. **Shaoqing Song:** Ideas, Formulation or evolution of overarching research goals and aims.

## Declaration of Competing Interest

The authors declare that they have no known competing financial interests or personal relationships that could have appeared to influence the work reported in this paper.

## Data Availability

No data was used for the research described in the article.

## Acknowledgements

This study was jointly supported by the National Natural Science Foundation of China (21871155 and 51972177), Natural Science Foundation of Ningbo City (2021J067) and SJLY2021010 of Ningbo University, the Fan 3315 Plan, and the Yongjiang Scholar Plan.

## Appendix A. Supporting information

Supplementary data associated with this article can be found in the online version at [doi:10.1016/j.apcatb.2022.121945](https://doi.org/10.1016/j.apcatb.2022.121945).

## References

- [1] W. Peschka, Liquid Hydrogen: Fuel of the Future, Springer Science & Business, Berlin, 2012.
- [2] X.R. Li, Y. Chen, Y. Tao, L. Shen, Z.M. Xu, Z.F. Bian, H.X. Li, Challenges of photocatalysis and their coping strategies, *Chem. Catal.* 2 (2022) 1315–1345.
- [3] Technology roadmap: hydrogen and fuel cells, International Energy Agency, Paris, 2015.
- [4] M. Sayed, J.G. Yu, G. Liu, M. Jaroniec, Non-noble plasmonic metal-based photocatalysts, *Chem. Rev.* 122 (2022) 10484–10537.
- [5] Y. Chen, M.J. Xu, J.Y. Wen, Y. Wan, Q.F. Zhao, X. Cao, Y. Ding, Z.L. Wang, H.X. Li, Z.F. Bian, Selective recovery of precious metals through photocatalysis, *Nat. Sustain.* 4 (2021) 618–626.
- [6] X. Li, J.G. Yu, M. Jaroniec, X.B. Chen, Cocatalysts for selective photoreduction of CO<sub>2</sub> into solar fuels, *Chem. Rev.* 119 (2019) 3962–4179.
- [7] M. Kotesh Kumar, G. Naresh, V. Vijay Kumar, B. Sai Vasista, B. Sasikumar, A. Venugopal, Improved H<sub>2</sub> yields over Cu-Ni-TiO<sub>2</sub> under solar light irradiation: behaviour of alloy nano particles on photocatalytic H<sub>2</sub>O splitting, *Appl. Catal. B Environ.* 299 (2021), 120654.
- [8] Z.M. Xu, X.M. Deng, Y. Chen, J.Y. Wen, L.Y. Shi, Z.F. Bian, Engineering a rapid charge transfer pathway for enhanced photocatalytic removal efficiency of hexavalent chromium over C<sub>3</sub>N<sub>4</sub>/NH<sub>2</sub>-UiO-66 compounds, *Sol. RRL* 5 (2021), 2000416.
- [9] V. Kumaravel, S. Mathew, J. Bartlett, S.C. Pillai, Photocatalytic hydrogen production using metal doped TiO<sub>2</sub>: a review of recent advances, *Appl. Catal. B Environ.* 244 (2019) 1021–1064.
- [10] Y. Chen, Q.Y. Qiao, J.Z. Cao, H.X. Li, Z.F. Bian, Precious metal recovery, *Joule* 5 (2021) 3097–3115.
- [11] F. Chen, H.W. Huang, L. Guo, Y.H. Zhang, T.Y. Ma, The role of polarization in photocatalysis, *Angew. Chem. Int. Ed.* 58 (2019) 10061–10073.
- [12] J.R. He, Y. Zhao, S.J. Jiang, S.Q. Song, Photocatalysis within intrinsic spontaneous polarization electric field, *Sol. RRL* 5 (2021), 2000446.
- [13] F. Chen, Z.Y. Ma, L.Q. Ye, T.Y. Ma, T.R. Zhang, Y.H. Zhang, H.W. Huang, Macroscopic spontaneous polarization and surface oxygen vacancies collaboratively boosting CO<sub>2</sub> photoreduction on Bi<sub>2</sub>O<sub>3</sub> single crystals, *Adv. Mater.* 32 (2020), 1908350.
- [14] L. Ju, J. Shang, X. Tang, L.Z. Kou, Tunable photocatalytic water splitting by the ferroelectric switch in a 2D AgBiP<sub>2</sub>Se<sub>6</sub> monolayer, *J. Am. Chem. Soc.* 142 (2020) 1492–1500.
- [15] K. Fischer, R. Gläser, A. Schulze, Nanoneedle and nanotubular titanium dioxide-PES mixed matrix membrane for photocatalysis, *Appl. Catal. B Environ.* 160 (2014) 456–464.
- [16] W.P. Zhao, Y.M. Wu, J. Xu, C.H. Gao, Effect of ethylene glycol on hydrothermal formation of calcium sulfate hemihydrate whiskers with high aspect ratios, *RSC Adv.* 5 (2015) 50544–50548.
- [17] H.B. Zhang, Y.Y. Liu, T. Chen, J.T. Zhang, J. Zhang, X.W. Lou, Unveiling the activity origin of electrocatalytic oxygen evolution over isolated Ni atoms supported on a N-doped carbon matrix, *Adv. Mater.* 31 (2019), 1904548.
- [18] Z.X. Lin, Y. Zhao, J.H. Luo, S.J. Jiang, C.Z. Sun, S.Q. Song, Apparent potential difference boosting directional electron transfer for full solar spectrum-irradiated catalytic H<sub>2</sub> evolution, *Adv. Funct. Mater.* 30 (2020), 1908797.
- [19] D.X. Yang, Z. Su, Y.F. Chen, K. Srinivas, J.Z. Gao, W.L. Zhang, Z.G. Wang, H.P. Lin, Electronic modulation of hierarchical spongy nanosheets toward efficient and stable water electrolysis, *Small* 17 (2021), 2006881.
- [20] C. Tang, R. Zhang, W.B. Lu, Z. Wang, D.N. Liu, S. Hao, G. Du, A.M. Asiri, X.P. Sun, Energy-saving electrolytic hydrogen generation: Ni<sub>2</sub>P nanoarray as a high-performance non-noble-metal electrocatalyst, *Angew. Chem. Int. Ed.* 56 (2017) 842–846.
- [21] H. Huang, Y. Zhao, Y.M. Bai, F.M. Li, Y. Zhang, Y. Chen, Conductive metal-organic frameworks with extra metallic sites as an efficient electrocatalyst for the hydrogen evolution reaction, *Adv. Sci.* 7 (2020), 2000012.
- [22] H.-J. Qiu, P. Du, K.L. Hu, J.J. Gao, H.L. Li, P. Liu, T. Ina, K. Ohara, Y. Ito, M. W. Chen, Metal and nonmetal codoped 3D nanoporous graphene for efficient bifunctional electrocatalysis and rechargeable Zn-air batteries, *Adv. Mater.* 31 (2019), 1900843.
- [23] X.L. Pan, X.H. Bao, Reactions over catalysts confined in carbon nanotubes, *Chem. Commun.* 47 (2008) 6271–6281.
- [24] J.P. Xiao, X.L. Pan, F. Zhang, H.B. Li, X.H. Bao, Size-dependence of carbon nanotube confinement in catalysis, *Chem. Sci.* 8 (2017) 278–283.
- [25] G. Liu, L. Ma, L.C. Yin, G.D. Wan, H.Z. Zhu, C. Chen, Y.Q. Yang, Y. Liang, J. Tan, H. M. Cheng, Selective chemical epitaxial growth of TiO<sub>2</sub> islands on ferroelectric PbTiO<sub>3</sub> crystals to boost photocatalytic activity, *Joule* 2 (2018) 1095–1107.
- [26] Y. Liu, S. Ye, H.C. Xie, J. Zhu, Q. Shi, N. Ta, R.T. Chen, Y.Y. Gao, H.Y. An, W. Nie, H.W. Jing, F.T. Fan, C. Li, Internal-field-enhanced charge separation in a single domain ferroelectric PbTiO<sub>3</sub> photocatalyst, *Adv. Mater.* 32 (2020), 1906513.
- [27] C.V. Dyck, T.J. Marks, M.A. Ratner, Chain length dependence of the dielectric constant and polarizability in conjugated organic thin films, *ACS Nano* 11 (2017) 5970–5981.
- [28] E.J.G. Santos, E. Kaxiras, Electric-field dependence of the effective dielectric constant in graphene, *Nano Lett.* 13 (2013) 898–902.
- [29] X.Y. Fan, K.R. Lai, L.C. Wang, H.S. Qiu, J. Yin, P.J. Zhao, S.L. Pan, J.B. Xua, C. Y. Wang, Efficient photocatalytic dechlorination of chlorophenols over a nonlinear optical material Na<sub>3</sub>VO<sub>2</sub>B<sub>6</sub>O<sub>11</sub> under UV-visible light irradiation, *J. Mater. Chem. A* 3 (2015) 12179–12187.
- [30] W.H. Nam, B.B. Kim, S.G. Seo, Y.S. Lim, J.Y. Kim, W.S. Seo, W.K. Choi, H.H. Park, J.Y. Lee, Structurally nanocrystalline-electrically single crystalline ZnO-reduced graphene oxide composites, *Nano Lett.* 14 (2014) 5104.
- [31] D.M. Tang, C.T. Shao, S.J. Jiang, C.Z. Sun, S.Q. Song, Graphitic C<sub>2</sub>N<sub>3</sub>: an allotrope of g-C<sub>3</sub>N<sub>4</sub> containing active azide pentagons as metal-free photocatalyst for abundant H<sub>2</sub> bubble evolution, *ACS Nano* 15 (2021) 7208–7215.
- [32] T. Tachikawa, M. Fujitsuka, T. Majima, Mechanistic insight into the TiO<sub>2</sub> photocatalytic reactions: design of new photocatalysts, *J. Phys. Chem. C* 111 (2007) 5259–5275.
- [33] W. Xun, Y.J. Wang, R.L. Fan, Q.Q. Mu, S. Ju, Y. Peng, M.R. Shen, Activating the MoS<sub>2</sub> basal plane toward enhanced solar hydrogen generation via in situ photoelectrochemical control, *ACS Energy Lett.* 6 (2021) 267–276.
- [34] H. Wang, W.X. Liu, X. He, P. Zhang, X.D. Zhang, Y. Xie, An excitonic perspective on low-dimensional semiconductors for photocatalysis, *J. Am. Chem. Soc.* 142 (2020) 14007–14022.
- [35] C.L. Hu, L. Zhang, J.L. Gong, Recent progress made in the mechanism comprehension and design of electrocatalysts for alkaline water splitting, *Energy Environ. Sci.* 12 (2019) 2620–2645.
- [36] P. Zhang, T. Wang, J.L. Gong, Current mechanistic understanding of surface reactions over water-splitting photocatalysts, *Chem* 4 (2018) 223–245.
- [37] V.M. Nikolic, S.L. Maslovarac, G.S. Tasic, T.P. Brdaric, P.Z. Lausevic, B.B. Radak, M. P.M. Kaninski, Kinetics of hydrogen evolution reaction in alkaline electrolysis on a Ni cathode in the presence of Ni-Co-Mo based ionic activators, *Appl. Catal. B: Environ.* 179 (2015) 88–94.
- [38] X.J. Chen, J. Wang, Y.Q. Chai, Z.J. Zhang, Y.F. Zhu, Efficient photocatalytic overall water splitting induced by the giant internal electric field of a g-C<sub>3</sub>N<sub>4</sub>/rGO/PDPD Z-scheme heterojunction, *Adv. Mater.* 33 (2021), 2007479.
- [39] T. Yu, T. Xie, W. Zhou, Y.Z. Zhang, Y.L. Chen, B.Y. Shao, W.Q. Guo, X. Tan, Fumaric acid assistant band structure tunable nitrogen defective g-C<sub>3</sub>N<sub>4</sub> fabrication for enhanced photocatalytic hydrogen evolution, *ACS Sustain. Chem. Eng.* 9 (2021) 7529–7540.
- [40] Z.Q. Zhao, R.V. Goncalves, S.K. Barman, E.J. Willard, E. Byle, R. Perry, Z.K. Wu, M. N. Huda, A.J. Moule, F.E. Osterloh, Electronic structure basis for enhanced overall water splitting photocatalysis with aluminum doped SrTiO<sub>3</sub> in natural sunlight, *Energy Environ. Sci.* 12 (2019) 1385–1395.
- [41] X.C. Zhang, T.Y. Liu, F. Zhao, N. Zhang, Y.H. Wang, In-situ-formed Cd and Ag<sub>2</sub>S decorated Cds photocatalyst with boosted charge carrier spatial separation for enhancing UV-vis-NIR photocatalytic hydrogen evolution, *Appl. Catal. B Environ.* 298 (2021), 120620.
- [42] S.C. Sun, G.Q. Shen, Z.C. Chen, L. Pan, X.W. Zhang, J.J. Zou, Harvesting urbach tail energy of ultrathin amorphous nickel oxide for solar-driven overall water splitting up to 680 nm, *Appl. Catal. B Environ.* 285 (2021), 119798.
- [43] C.W. Yang, J.Q. Qin, S. Rajendran, X.Y. Zhang, R.P. Liu, WS<sub>2</sub> and C-TiO<sub>2</sub> nanorods acting as effective charge separators on g-C<sub>3</sub>N<sub>4</sub> to boost visible-light activated hydrogen production from seawater, *ChemSusChem* 11 (2018) 4077–4085.
- [44] Y.Q. Wu, Q. Wu, Q.Q. Zhang, Z.Z. Lou, K.F. Liu, Y.D. Ma, Z.Y. Wang, Z.K. Zheng, H. F. Cheng, Y.Y. Liu, Y. Dai, B.B. Huang, P. Wang, Organometal halide perovskite

supported Pt single-atom photocatalyst for H<sub>2</sub> evolution, *Energy Environ. Sci.* 15 (2022) 1271.

[45] Y. Zhao, C.M. Ding, J. Zhu, W. Qin, X.P. Tao, F.T. Fan, R.G. Li, C. Li, A hydrogen farm strategy for scalable solar hydrogen production with particulate photocatalysts, *Angew. Chem. Int. Ed.* 59 (2020) 9653–9658.

[46] X.L. Song, G.F. Wei, J. Sun, C.D. Peng, J.L. Yin, X. Zhang, Y.L. Jiang, H.H. Fei, Overall photocatalytic water splitting by an organolead iodide crystalline material, *Nat. Catal.* 3 (2020) 1027–1033.

[47] Y. Qi, Y. Zhao, Y.Y. Gao, D. Li, Z. Li, F.X. Zhang, C. Li, Redox-based visible-light-driven Z-scheme overall water splitting with apparent quantum efficiency exceeding 10%, *Joule* 2 (2018) 2393–2402.

[48] S. Sun, T. Hisatomi, Q. Wang, S.S. Chen, G.J. Ma, J.Y. Liu, S. Nandy, T. Minegishi, M. Katayama, K. Domen, Efficient redox-mediator-free Z-scheme water splitting employing oxysulfide photocatalysts under visible light, *ACS Catal.* 8 (2018) 1690–1696.

[49] Q. Wang, T. Hisatomi, Q.X. Jia, H. Tokudome, M. Zhong, C.Z. Wang, Z.H. Pan, T. Takata, M. Nakabayashi, N. Shibata, Y.B. Li, L.D. Sharp, A. Kudo, T. Yamada, K. Domen, Scalable water splitting on particulate photocatalyst sheets with a solar-to-hydrogen energy conversion efficiency exceeding 1%, *Nat. Mater.* 15 (2016) 611–615.

[50] M.S. Zhu, X.Y. Cai, M. Fujitsuka, J.Y. Zhang, T. Majima, Au/La<sub>2</sub>Ti<sub>2</sub>O<sub>7</sub> nanostructures sensitized with black phosphorus for plasmon-enhanced photocatalytic hydrogen production in visible and near-infrared light, *Angew. Chem. Int. Ed.* 56 (2017) 2064–2068.

[51] X.L. Zhao, S. Chen, H.J. Yin, S.Y. Jiang, K. Zhao, J. Kang, P.F. Liu, L.X. Jiang, Z. J. Zhu, D.D. Cui, P.R. Liu, X.J. Han, H.G. Yang, H.J. Zhao, Perovskite microcrystals with intercalated monolayer MoS<sub>2</sub> nanosheets as advanced photocatalyst for solar-powered hydrogen generation, *Matter* 3 (2020) 935–949.

[52] F.X. Tong, X.Z. Liang, M. Liu, Z.Y. Wang, Y.Y. Liu, P. Wang, H.F. Cheng, Y. Dai, Z. K. Zheng, B.B. Huang, Plasmon-enhanced water activation for hydrogen evolution from ammonia-borane studied at a single-particle level, *ACS Catal.* 12 (2022) 3558–3565.